Brightly Luminescent and Color-Tunable Colloidal $CH_3NH_3PbX_3$ (X = Br, I, Cl) Quantum Dots: Potential Alternatives for Display Technology

Feng Zhang,[†] Haizheng Zhong,[*,†] Cheng Chen,[§] Xian-gang Wu,[†] Xiangmin Hu,[‡] Hailong Huang,[‡] Junbo Han,[§] Bingsuo Zou,[‡] and Yuping Dong[†]

[†]Beijing Key Laboratory of Nanophotonics and Ultrafine Optoelectronic Systems, School of Materials Science & Engineering, Beijing Institute of Technology, 5 Zhongguancun South Street, Haidian District, Beijing 100081, China, [‡]Micro Nano Technology Center, School of Physics, Beijing Institute of Technology, 5 Zhongguancun South Street, Haidian District, Beijing 100081, China, and [§]Wuhan National High Magnetic Field Center and School of Physics, Huazhong University of Science and Technology, Wuhan 430074, China

ABSTRACT Organometal halide perovskites are inexpensive materials with desirable characteristics of color-tunable and narrow-band emissions for lighting and display technology, but they suffer from low photoluminescence quantum yields at low excitation fluencies. Here we developed a ligand-assisted reprecipitation strategy to fabricate brightly luminescent and color-tunable colloidal $CH_3NH_3PbX_3$ (X = Br, I, Cl) quantum dots with absolute quantum yield up to 70% at room temperature and low excitation fluencies. To illustrate the photoluminescence enhancements in these quantum dots, we conducted comprehensive composition and surface characterizations and determined the time- and temperature-dependent photoluminescence spectra. Comparisons between small-sized $CH_3NH_3PbBr_3$ quantum dots (average diameter 3.3 nm) and corresponding micrometer-sized bulk particles (2−8 μm) suggest that the intense increased photoluminescence quantum yield originates from the increase of exciton binding energy due to size reduction as well as proper chemical passivations of the Br-rich surface. We further demonstrated wide-color gamut white-light-emitting diodes using green emissive $CH_3NH_3PbBr_3$ quantum dots and red emissive $K_2SiF_6:Mn^{4+}$ as color converters, providing enhanced color quality for display technology. Moreover, colloidal $CH_3NH_3PbX_3$ quantum dots are expected to exhibit interesting nanoscale excitonic properties and also have other potential applications in lasers, electroluminescence devices, and optical sensors.

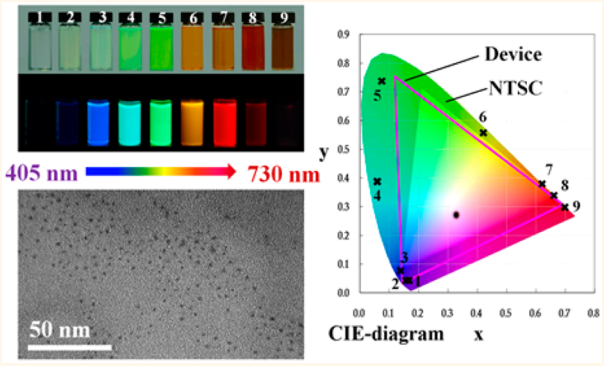

KEYWORDS: organometal halide perovskites · quantum dots · exciton · photoluminescence · light-emitting diode

The lighting and display technologies are looking for color-tunable and narrow-band emissive materials to enhance the color performance of lighting and display systems.[1−3] Colloidal quantum dots (QDs) emerge as next generation candidates with color-tunable and narrow-band emissions as well as high photoluminescence quantum yields (PLQYs).[3,4] Recently, notable success has been made on QDs based on wide-color gamut backlighting systems for display applications.[5] However, the commercialization still suffers from the lack of inexpensive and high-quality materials.[5] Organometal halide perovskites ($CH_3NH_3PbX_3$, where X = Br, I, Cl) have attracted great attention due to their excellent performance in solar energy conversion as well as the interesting excited-state dynamics.[6−12] Because of the wide wavelength tunability (400−800 nm) and narrow-band emission (full width at half-maximum, fwhm ~20 nm), organometal halide perovskites have also been of great interest as emissive components in phosphor-converted white-light-emitting diodes (pc-WLED), low-threshold lasers, and electroluminescence (EL) devices.[13−17] However, owing to the presence of nonradiative pathways through sub-band defect states, high PLQYs and

* Address correspondence to hzzhong@bit.edu.cn.

Received for review February 19, 2015 and accepted March 30, 2015.

Published online March 30, 2015
10.1021/acsnano.5b01154

bright EL emissions can be only achieved at high excitation fluencies or high current density, which have been an obstacle for the device application.[18,19] It has been suggested that the PL emission of organometal halide perovskites could be enhanced by controlling their size dimension[20,21] or proper passivation of the surface vacancies.[22] By gaining insight into the PL enhancements, we herein demonstrate a combined size tuning and chemical passivation strategy to overcome the problem of trap defects.

The role of defects in semiconductor materials is very essential in controlling their electrical and optical properties.[23] Theoretical calculations show that organometal halide perovskites have complicated intrinsic defects.[24,25] Considering the size effects, the number of intrinsic defects should decrease with the volume shirking and may be further reduced due to the autoexcluding effects.[26] However, surface defects are dominant in nanosized materials due to the large surface to volume ratio. Considering the increased exciton binding energy in small-sized QDs, the PL emission is more likely to originate from the exciton recombination rather than the recombination from free electrons and holes.[27] If the surface defects of nanosized organometal halide perovskites can be well-passivated, it could be possible to obtain highly luminescent nanoparticles with fewer defects, which potentially have high PLQYs at room temperature and low excitation density.[19] This has been evidenced by recent works, which reported the fabrication of $CH_3NH_3PbBr_3$ and $CsPbX_3$ nanocrystals and with high PLQYs up to ~80% by adapting the heating up injection method from II–VI QDs.[28,29] Because $CH_3NH_3PbBr_3$ was predicted to have an exciton Bohr radius of ~2.0 nm,[30] smaller-size nanoparticles with a diameter less than 4 nm may exhibit enhanced quantum confinement effects and have been of great interest for fundamental study. We report here a ligand-assisted reprecipitation (LARP) technique, which is convenient and versatile for the fabrication of $CH_3NH_3PbX_3$ QDs at room temperature.

Reprecipitation method through solvent mixing is a simple technique that can prepare organic nanoparticles or polymer dots simultaneously through the solvent mixing.[31−33] Introduction of capping ligands on the surface of nanoparticles has been extensively investigated and has become an increasingly mature strategy to control their size and morphology.[34,35] This inspired us to control the crystallization of $CH_3NH_3PbX_3$ in the reprecipitation process by varying the surface ligands. Without using long-chain ligands, the reprecipitation method gives micrometer-sized particles with very low PLQYs (<0.1%). By incorporating *n*-octylamine and oleic acid as coligands into the reprecipitation process, we produced brightly luminescent colloidal $CH_3NH_3PbBr_3$ QDs with absolute PLQYs up to 70%. To illustrate the PL enhancements in these $CH_3NH_3PbBr_3$ QDs, we conducted comparative studies between $CH_3NH_3PbBr_3$ QDs (average diameter 3.3 nm) and corresponding micrometer-sized particles. The increase of exciton binding energy due to size reduction as well as proper chemical passivations of the Br-rich surface is clarified and discussed. We further demonstrate the wide gamut prototype LED devices.

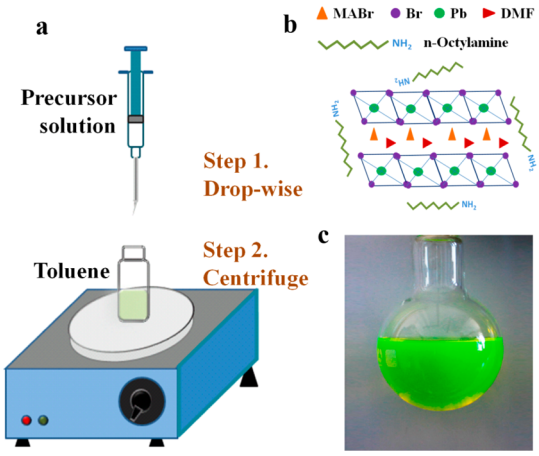

Figure 1. (a) Schematic illustration of the reaction system and process for LARP technique. (b) Schematic illustration of starting materials in the precursor solution. (c) Typical optical image of colloidal $CH_3NH_3PbBr_3$ solution.

RESULTS AND DISCUSSION

The LARP synthesis is accomplished by simply mixing a solution of $CH_3NH_3PbBr_3$ precursors in good solvent (*N*-dimethylformamide, DMF) into a vigorously stirred poor solvent (toluene, hexane, *etc.*) with long-chain organic ligands, which subsequently result in the controlled crystallization of precursors into colloidal nanoparticles. Figure 1 schematically illustrates the typical fabrication process of the LARP technique. In a typical synthesis of $CH_3NH_3PbBr_3$ QDs, a mixture of $PbBr_2$, CH_3NH_3Br, *n*-octylamine, and oleic acid was dissolved into DMF to form a clear precursor solution. In the precursor solution, DMF acts as a good solvent to dissolve the inorganic salts and small molecules. The formation of free-standing layered precursors in DMF has been previously discussed and is schematically shown in Figure 1b.[36] A fixed amount of precursor solution was dropped into toluene under vigorous stirring. After that, a yellow-green colloidal solution was formed, indicating the aggregation process of the precursors into nanoparticles. The colloidal solution in toluene was centrifuged at 7000 rpm to discard large particles. As shown in Figure 1c, the resulting colloidal solution is of high quality, indicating the formation of small-sized nanoparticles.

To understand the role of long-chain ligands in the formation process, we conducted contrast experiments with various reagents in the precursor solution. Without *n*-octylamine added, the precursors undergo fast crystallization and aggregated into large particles

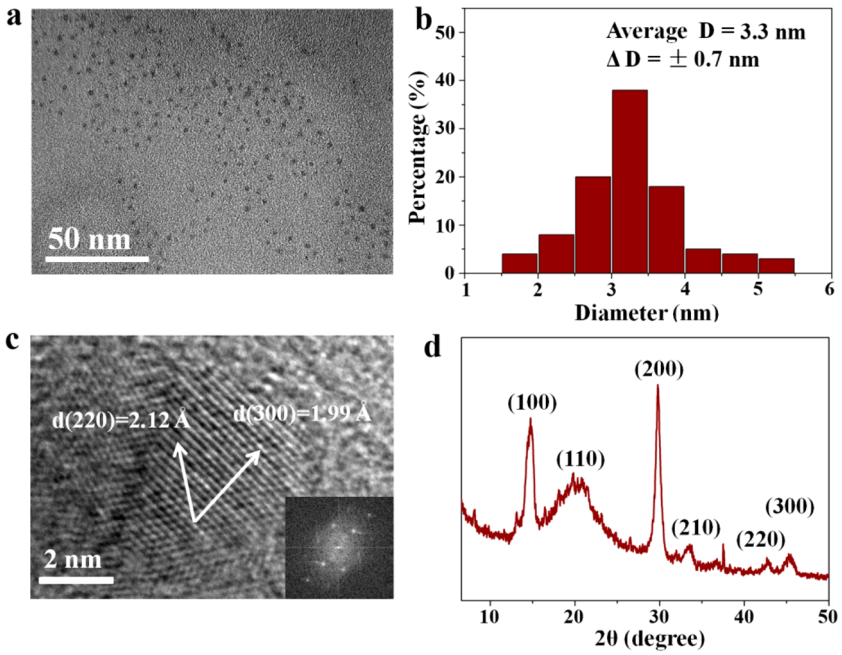

Figure 2. (a) TEM image of colloidal $CH_3NH_3PbBr_3$ QDs. (b) Analysis of size distribution for the sample shown in panel a. (c) HRTEM image of a typical $CH_3NH_3PbBr_3$ QD. The inset in the bottom right corner is the corresponding FFT image. (d) XRD patterns of $CH_3NH_3PbBr_3$ QDs. The corresponding Miller indexes are labeled at the top of the diffraction peaks.

and subsequently precipitated from the solution. The use of other alkylamines with longer chains, including dodecylamine, hexadecylamine, and hexylamine, can also control the crystallization process and give colloidal QD solutions. Without using oleic acid, a luminescent colloidal QDs solution can be also obtained; however, the colloidal solution became cloudy after storage for 24 h (see Figure S1 in the Supporting Information). Moreover, other long-chain alkyl acids (octanoic acid, butyric acid, *etc.*) are also suitable to stabilize the formed colloidal $CH_3NH_3PbBr_3$ QDs. Based on the above observations, it is assumed that the crystallization process is controlled by the supersaturation induced by the solubility change with solvent mixing. These results also revealed that *n*-octylamine controls the kinetics of crystallization, which mainly contributes to the size control of QDs. Oleic acid plays an important role in suppressing the QD aggregation effects and contributes to the colloidal stability. Because of the high volume to surface ratio of nanoparticles, the stabilization effects of oleic acid may be explained by the charge equilibrium.

Figure 2a,b shows a typical transmission electron microscopy (TEM) image of $CH_3NH_3PbBr_3$ QDs as well as the size distribution; it is observed that typical $CH_3NH_3PbBr_3$ QDs have an average diameter of 3.3 nm with a size deviation of ±0.7 nm. In order to analyze the phase structure, X-ray diffraction (XRD) patterns and high-resolution transmission electron microscopy (HRTEM) determinations were applied to characterize the obtained samples. The XRD data (Figure 2d) show that the sample has a well-defined three-dimensional structure, which confirmed the formation of $CH_3NH_3PbBr_3$ QDs. Detailed information on the lattice spacing is listed in Supporting Information Table S1. To further elucidate the crystal structure, we also characterized the micrometer-sized $CH_3NH_3PbBr_3$ particles (the preparation is described in the Materials and Methods section), which were are the bulk counterpart. Figures S2 and S3 present the SEM images as well as the XRD patterns of the micrometer-sized $CH_3NH_3PbBr_3$ particles. In comparison to the micrometer-sized particles, we observed obvious broadening of the diffraction peaks corresponding to the small size of colloidal QDs. From the HRTEM image (Figure 2c) and the fast Fourier transformation (FFT) image (inset of Figure 2c), interplanar distances of 1.99 and 2.12 Å corresponding to the (300) and (220) crystal faces, respectively, can be easily identified, which are consistent with the XRD results.

According to the structural formula, $CH_3NH_3PbBr_3$ has an ideal Br/Pb molar ratio close to ~3.0 for bulk materials. The energy-dispersive spectroscopy (EDS) measurement shows that micrometer-sized $CH_3NH_3PbBr_3$ particles have a Br/Pb molar ratio of 3.1 (see Table S2 in the Supporting Information), which agrees well with the stoichiometry. As it is widely recognized, surface atoms play a vital role in determining the physical properties of colloidal QDs.[37−39] Small-sized QDs are usually nonstoichiometric due to the anion- or cation-rich surface.[37] Figure 3a shows the molecular structural model of $CH_3NH_3PbBr_3$ QDs. Because surface atoms occupy a large ratio in nanosized particles, the Br/Pb molar ratio should vary with the size decrease due to the enhanced influence from surface atoms. The Br/Pb molar ratio of $CH_3NH_3PbBr_3$ QDs was

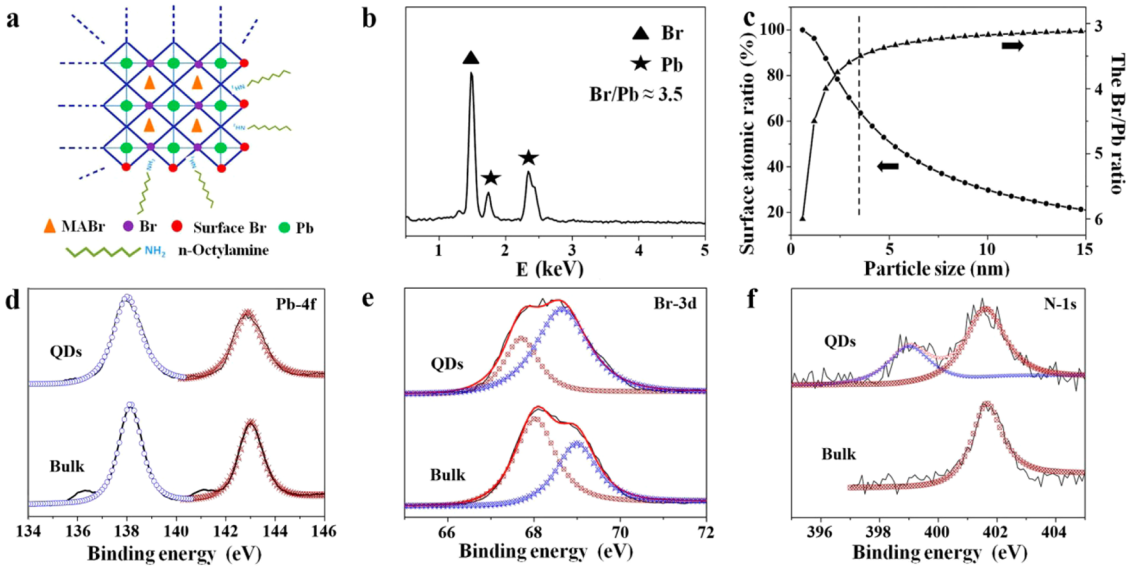

Figure 3. (a) Molecular structural model. (b) EDS spectra of a typical sample of $CH_3NH_3PbBr_3$ QDs. (c) Relationship between the percentage of the surface atom and Br/Pb ratio with particle size. (d–f) XPS spectra corresponding to Pb 4f (d), Br 3d (e), and N 1s (f) of $CH_3NH_3PbBr_3$ QDs and bulk materials.

also determined by applying EDS measurements. As shown in Figure 3b, the as-fabricated 3.3 nm $CH_3NH_3PbBr_3$ QDs have a Br/Pb molar ratio of 3.5, implying a Br-rich surface. If we assumed that the obtained $CH_3NH_3PbBr_3$ QDs consisted of ideal $[PbBr_6]^{4-}$ octahedron unit cell, the Br atom should account for a large percentage on the surface compared with the corresponding bulk material. Therefore, we conduct simple modeling to describe the correlations between QDs' size and surface stoichiometry as well as the surface atomic percentage. This model assumes that the resulting QDs are cubic cubes with stoichiometric composition within the dots and that any excess ions exist on the surface (see Figure S4 in the Supporting Information). Figure 3c shows the variation of Br/Pb molar ratio and surface atomic percentage with particle size. It is worth noting that the 3.3 nm $CH_3NH_3PbBr_3$ QDs are predicted to have a Br/Pb molar ratio of 3.55. The prediction is in good agreement with the EDS results (~3.5), confirming the existence of a Br-rich surface.

X-ray photoelectron spectroscopy (XPS) determinations were also performed to further investigate the surface properties of colloidal $CH_3NH_3PbBr_3$ QDs and micrometer-sized particles. Figure 3d–f shows the XPS spectra of Pb 4f, Br 3d, and N 1s spectra for resulting QDs and the corresponding bulk counterpart. The main peaks of Pb 5f and Br 4d in the QDs' spectra have binding energy positions similar to those of the bulk micrometer-sized particles. The presence of small peaks in the lower binding energy is noted for the bulk micrometer-sized particles, implying the absence of Pb ions on the QDs' surface. The Br 3d peaks can be fitted into two peaks with binding energies of 67.7 and 68.7 eV for 3.3 nm QDs and 68.0 and 69.0 eV for micrometer-sized particles, corresponding to the inner and surface ions, respectively. The intensity ratio difference between these two peaks and the peak between QDs and the bulk counterpart can be attributed to the Br-rich surface of QDs. The N 1s spectrum of $CH_3NH_3PbBr_3$ QDs shows two peaks with binding energy at 399.0 and 401.6 eV, implying the two existing chemical conditions of the N element. When XPS spectra of micrometer-sized particles were compared, the peak with a binding energy of 399.0 eV of $CH_3NH_3PbBr_3$ QDs can be attributed to the presence of *n*-octylamine, while the peak with a binding energy of 401.6 eV originates from methylamine. The presence of *n*-octylamine confirmed that *n*-octylamine acts as a capping ligand to control the crystallization process and to account for the formation of colloidal QDs. In all, $CH_3NH_3PbBr_3$ QDs have a Br-rich surface with *n*-octylamine and oleic acid capping.

We further studied the optical properties of $CH_3NH_3PbBr_3$ QDs and corresponding micrometer-sized particles. Figure 4a shows the absorption (red) and emission (green) spectra of $CH_3NH_3PbBr_3$ QDs. The UV–vis absorption spectrum of $CH_3NH_3PbBr_3$ QDs has a band edge at 505 nm. In the PL spectrum, a sharp emission peak at 515 nm with a fwhm value of only 21 nm (~96 meV) can be observed, indicating the superior color saturation than that reported for CdSe- or InP-based QDs.[5,34] The sample has a relatively smaller Stokes shift of ~49 meV, implying that the PL emission of QDs originates from direct exciton recombination. In addition, the emission peak was ~30 nm (~131 meV) blue-shifted compared to that of $CH_3NH_3PbBr_3$ bulk materials.[20] Because of the smaller size of $CH_3NH_3PbBr_3$ QDs relative to the 2-fold exciton Bohr radius (~4.0 nm),[30] the observed blue

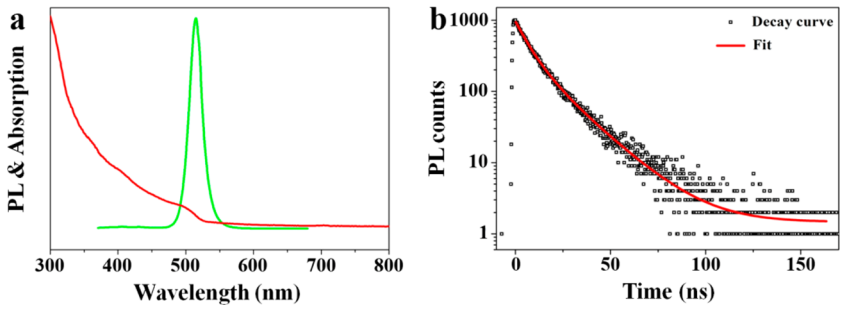

Figure 4. (a) UV−vis absorption and PL emission spectra. (b) Time-resolved PL decay and fitting curve of a typical sample of $CH_3NH_3PbBr_3$ QDs in toluene.

shift of $CH_3NH_3PbBr_3$ QDs could be explained by the quantum confinement effect. However, the $CH_3NH_3PbBr_3$ QDs exhibit less quantum confinement effects than the well-known CdSe- and InP-based QDs,[5] which give them the advantage of slight batch to batch variations. The absolute PLQYs of diluted QDs solutions were determined using a fluorescence spectrometer with an integrated sphere excited at a wavelength of 450 nm. The PLQYs of 50−70% were recorded for the samples from different batches, which are comparable to nonshelled CdSe QDs.[34,37] The high PLQYs indicated the reduction of nonradiative decay in high-quality smaller $CH_3NH_3PbBr_3$ QDs. To gain more insight into the exciton recombination dynamics, time-resolved PL spectra were measured, as shown in Figure 4b. The PL decay can be described by biexponential fitting (eq 1), giving a short-lived PL lifetime (τ_1) of 6.6 ns with a percentage of 63.6% and long-lived PL lifetime (τ_2) of 18.0 ns with a percentage of 36.4%.

$$A(t) = A_1 \exp\left(\frac{-t}{\tau_1}\right) + A_2 \exp\left(\frac{-t}{\tau_2}\right) \quad (1)$$

Compared to bulk films (average PL lifetime of ~100 ns),[40] the average PL lifetime of colloidal $CH_3NH_3PbBr_3$ QDs was greatly reduced with decreasing size. This suggests that the PL decay of colloidal $CH_3NH_3PbBr_3$ QDs mainly took place through exciton radiative recombination. The biexponential decay behavior strongly suggested that two different species are involved in the emission. According to the study of surface-related emission in highly luminescent CdSe QDs,[41] the short-lived PL lifetime is attributed to the recombination of initially generated excitons upon light absorption, while the long-lived component may correlate to the exciton recombination with the involvement of surface states due to the stable excitons at room temperature. However, this may need further spectroscopic study.

According to the statements in the introduction, the PL enhancements of $CH_3NH_3PbBr_3$ QDs are correlated with the increased exciton binding energy and/or the reduced density of defect states. To further verify the mechanism of PL enhancement, low-temperature-dependent PL spectra were obtained on colloidal QDs and corresponding micrometer-sized particles. As shown in Figure 5a,b, a pseudocolor map of the temperature-dependent PL spectra illustrates the evolution of PL emission with temperature from 5 to 300 K for colloidal QDs and corresponding bulk material. Because of the high PLQYs of QDs, the evolution of PL spectra at higher temperatures from 300 to 400 K was also studied to elucidate the potential integration into LED devices (see Figure 5c).[42] To gain more insights, these temperature-dependent PL spectra were analyzed in detail. As shown in Figure S5 in the Supporting Information, the absence of defect-related emission in the PL spectra of QDs at 5 K demonstrated that the surface defect states of resulting QDs are well-passivated. To further compare the PL properties, we plotted the photon energy of PL emission with increasing temperature (see Figure S6a in the Supporting Information). Both of the $CH_3NH_3PbBr_3$ QDs and micrometer-sized particles exhibit obvious blue shifts in the PL spectra with increasing temperature. It is observed that the micrometer-sized particles have a transition point around 100 K. Similar behaviors were also observed in phase transitions on $CH_3NH_3PbI_3$ porous films.[43] In comparison to the bulk counterpart, $CH_3NH_3PbBr_3$ QDs only slightly varied in the range from 4 to 50 K but gradually increased thereafter with increasing temperature. This unusual phenomenon is counterintuitive with the temperature-dependent behavior in most of the semiconductors but is in accordance with the recent observations in lead- and copper-salt-based semiconductors.[44]

Comparison of the integrated PL evolution between QDs and the bulk counterpart implies that the excitonic binding energy greatly increases with the size reduction, and the reduction of trap defects reduces the exciton migration into traps states. As shown in Figure S6b, the integrated PL intensity shows a different temperature-dependent evolution. The integrated PL intensity of QDs first decreased in the temperature range of 4−120 K, slightly varied from 100 to 273 K, and decreased to 70% of the initial value (room temperature) at the high temperature of 300−400 K. In contrast, the bulk material exhibited an exponential drop in the temperature before ~100 K and became nonluminescent thereafter. To extract the exciton

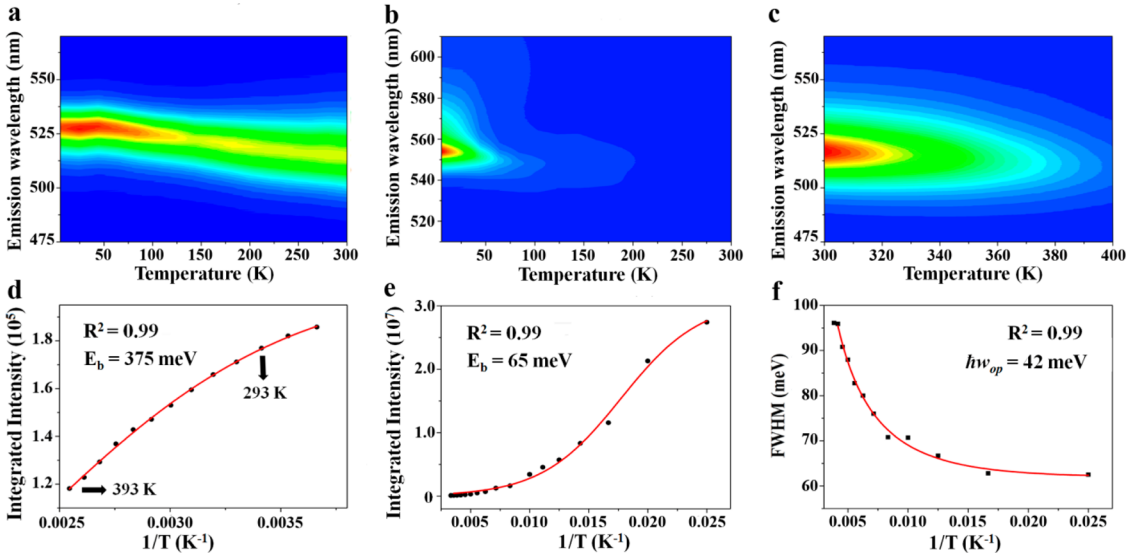

Figure 5. Pseudocolor maps of temperature-dependent PL spectra. (a) $CH_3NH_3PbBr_3$ QDs (5−300 K). (b) Corresponding bulk material (5−300 K). (c) $CH_3NH_3PbBr_3$ QDs (300−400 K). The PL intensity is represented by the color. The plots of integrated PL emission intensity as a function of temperature. (d) QDs (273−393 K). (e) Bulk material (50−300 K). (f) Plot of fwhm as a function of temperature for $CH_3NH_3PbBr_3$ QDs.

binding energy, Figure 5d,e plots the integrated PL emission intensity as a function of temperature for QDs (273−393 K) and bulk material (50−300 K) in their corresponding temperature range. The curves can be fitted using eq 2[43]

$$I(T) = \frac{I_0}{1 + Ae^{-E_b/k_BT}} \quad (2)$$

in which I_0 is the intensity at 0 K, E_b is the exciton binding energy, and k_B is the Boltzmann constant. From the fitting analysis, the QDs has a large exciton binding energy of ∼375 meV, while the bulk counterpart has an E_b of ∼65 meV, which is close to the previously reported values of 76 meV estimated from the magnetic absorption spectra.[30] Although the exciton binding energy of bulk $CH_3NH_3PbBr_3$ is large enough to show the excitonic effect at room temperature, previous works have demonstrated that recombination of bulk $CH_3NH_3PbBr_3$ was dominated by the recombination of free electrons and holes.[19] This has been attributed to the overestimation of exciton binding energy based on low-temperature experiments.[43] In our work, the exciton binding energy of QDs was evaluated by fitting the high temperature (300−400 K) spectroscopic results. Importantly, the relative 5.8-fold increase of exciton binding energy confirmed that the PL emissions of QDs mainly took place through exciton recombination rather than the recombination of free electrons and holes due to the enhanced exciton stability.

A detailed analysis of the temperature dependence of the PL peak broadening can provide information on the exciton−phonon coupling in QDs, which also strongly influences the excitonic PL emissions. The temperature-dependent fwhm of PL emissions for QDs (Figure 5f) can be fitted to extract optical phonon energy by adapting the independent Boson model (eq 3).[43]

$$\Gamma(T) = \Gamma_0 + \sigma T + \frac{\Gamma_{op}}{e^{\hbar\omega_{op}/k_BT} - 1} \quad (3)$$

in which the first term, Γ_0, is the inhomogeneous broadening contribution and σ and Γ_{op} describe the interactions of exciton−acoustic phonon and exciton−optical phonon contributions to the line width broadening, respectively. The fitting analysis shows that the optical phonon is mainly involved in the exciton−phonon interaction for $CH_3NH_3PbBr_3$ QDs. The optical phonon energy ($\hbar\omega_{op}$) is calculated to be ∼42.2 meV, implying strong exciton−phonon interactions. The extracted phonon energy is in accordance with the unresolved vibration energy (∼340 cm^{-1}) in the Raman spectrum.[45] In addition, the high optical phonon energy also agrees well with the thermal antiquenching effects at higher temperature.[46]

On the basis of the above discussions, it is obvious that the excitonic properties of $CH_3NH_3PbBr_3$ strongly depend on their size dimension and surface properties. Table S3 in the Supporting Information summarizes the characteristics of $CH_3NH_3PbBr_3$ QDs and micrometer-sized particles. With decreasing size, the increased exciton binding energy in QDs enables the generation of stable excitons at room temperature and influences the exciton recombination radiations. The observed blue shift and significant increase of PLQYs should correlate with the large exciton binding energy and Br-rich surface. Further works will focus on the size and surface control as well as the investigation of the correlations between structure and physical properties.

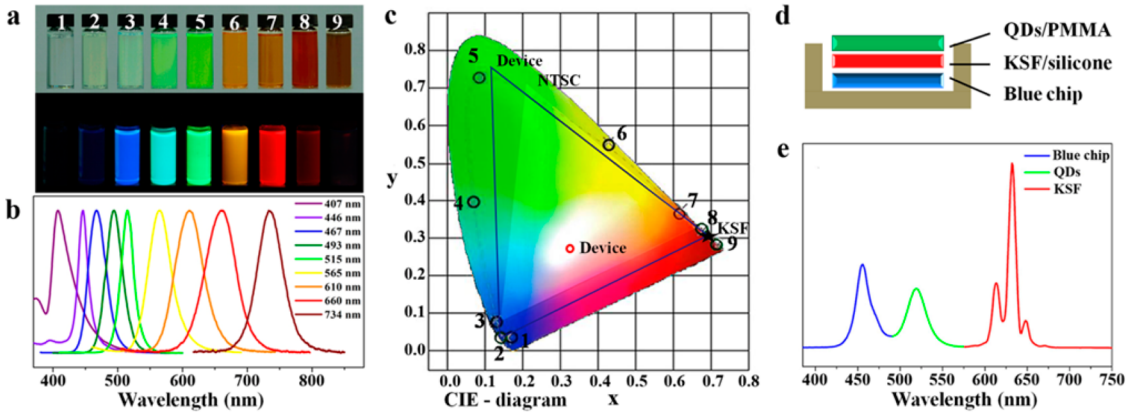

Figure 6. Color-tunable $CH_3NH_3PbX_3$ QDs and wide-color gamut pc-WLED devices. (a) Optical images of $CH_3NH_3PbX_3$ QDs (nos. 1−9) under ambient light and a 365 nm UV lamp. (b) PL emission spectra of $CH_3NH_3PbX_3$ QDs. (c) CIE color coordinates corresponding to the $CH_3NH_3PbX_3$ QDs (no. 1−9, black circle), pc-WLED devices (blue lines), and NTSC standard (bright area). (d,e) Schematic diagram and EL spectra of pc-WLED devices using green emissive $CH_3NH_3PbBr_3$ QDs and red emissive rare-earth phosphor KSF.

This simple LARP technique can be easily extended to fabricate colloidal $CH_3NH_3PbX_3$ QDs through halide substitutions. By simple mixing of PbX_2 salts in the precursors, we fabricated a series of colloidal $CH_3NH_3PbX_3$ QDs with tunable compositions (see Table S4 in the Supporting Information). Figure 6a,b shows the optical images of these samples under sunlight and a 365 nm UV lamp. As shown in Figure 6b and Figure S7, the absorption and PL spectra can be finely tuned from 407 to 734 nm by varying the composition of cations (X = Br, Cl, and I). The color coordinates of these samples were labeled as black circles in the commission international de L'Eclarage (CIE) chromaticity diagram (see Figure 6c), showing high color saturation due to their relative narrow emissions (fwhm = 20−50 nm). It noteworthy that colloidal $CH_3NH_3PbBr_3$ QDs with iodide substitution are very sensitive to air exposure. A similar phenomenon has also been observed in bulk films, which can be explained by the larger iodide-atom-induced structural deviation from the cubic phase.[47] The resulting Cl-substituted samples were further characterized by applying TEM and XRD measurements (see Figures S8 and S9 in the Supporting Information). These Cl-substituted QDs have size and structures similar to those of $CH_3NH_3PbBr_3$ QDs.

The available high-quality and stable colloidal $CH_3NH_3PbBr_3$ QDs with saturated green emission provide the opportunities to explore their use in display technology. To demonstrate their potential use in display technology, wide-color gamut prototype pc-WLED devices were fabricated by combing green emissive $CH_3NH_3PbBr_3$ QDs and red emissive rare-earth phosphor $K_2SiF_6:Mn^{4+}$ (KSF) with blue emissive GaN chips. Figure 6d,e shows the illustrative structure of pc-WLED devices and their corresponding EL spectrum. The optimized device has a luminous efficiency of 48 lm/W at a current density of 4.9 mA with a coordinate value of (0.33, 0.27) (see Table S5 in the Supporting Information). As shown in Figure 6c, the pc-WLED device covered a much larger area than the color space of the National Television Systems Committee (~130% of NTSC 1931) standard with a matching rate of 96%. The color rendition is superior to the performance of previously reported CdSe QD-based LEDs.[48] These results reflect great potential applications to fabricate wide-color gamut display devices.

CONCLUSIONS

In summary, we developed a simple and versatile LARP technique for the fabrication of brightly luminescent colloidal $CH_3NH_3PbX_3$ QDs with absolute PLQYs of 50−70%. The LARP technique is low cost and convenient for scale-up fabrications. The as-fabricated $CH_3NH_3PbBr_3$ QDs are nonstoichiometric due to the Br-rich surface. The proper chemical passivations of *n*-octylamine and oleic acid on the surface provide good colloidal stability. Moreover, the analysis of temperature-dependent PL spectra revealed that the 3.3 nm $CH_3NH_3PbBr_3$ QDs have an exciton binding energy of ~375 meV and an optical phonon energy of ~42 meV. The intense increase of exciton binding energy in QDs and their proper surface passivations account for the PL enhancements in $CH_3NH_3PbX_3$ QDs. Importantly, the combination of narrow emission with a fwhm of 20−50 nm, wide wavelength tunability of 400−750 nm, as well as high absolute PLQYs up to 70% provides potential alternatives with highly desirable characteristics for display technology. Using green emissive colloidal $CH_3NH_3PbBr_3$ QDs and red emissive rare-earth phosphor KSF, we fabricated wide-color gamut light-emitting prototype devices, which open up the possibility to improve the color performance of display technology. Moreover, colloidal $CH_3NH_3PbX_3$ QDs are also expected to exhibit interesting excitonic properties

because of the intermediate dielectronic constants between inorganic and organic materials.[49] Finally, the available brightly luminescent colloidal $CH_3NH_3PbX_3$ QDs add new family members to the field of QDs and will open the door to a range of applications, including lasers, EL devices, as well as optical sensors.

MATERIALS AND METHODS

Materials. All reagents were used as received without further purification: $PbCl_2$ (lead(II) chloride, 99%, Alfa Aesar), $PbBr_2$ (lead(II) bromide 99%, Aladdin), PbI_2 (lead(II) iodide 98.5%, Alfa Aesar), methylamine (CH_3NH_2, 33 wt % in absolute ethanol, Aladdin), *n*-octylamine (≥99%, Aladdin), hydrochloric acid (HCl, 37 wt % in water, Aladdin), hydrobromic acid (HBr, 48 wt % in water, Aladdin), hydriodic acid (HI, 57 wt % in water, Alfa Aesar), oleic acid (≥90%, Alfa Aesar), *N*,*N*-dimethylformamide (analytical grade, Beijing Chemical Reagent Co., Ltd., China), dimethyl sulfoxide (DMSO, analytical grade, Beijing Chemical Reagent Co., Ltd., China), toluene (analytical grade, Beijing Chemical Reagent Co., Ltd., China), K_2SiF_6:Mn^{4+} (KSF, Beijing Yuji Science & Technology Co., Ltd., China), poly(methyl methacrylate) (PMMA, average MW ~35 000, Alfa Aesar).

Synthesis of CH_3NH_3X (X = Cl, Br, or I). CH_3NH_3X (X = Cl, Br, or I) was synthesized by reaction of the methylamine with the corresponding acid. First, methylamine in absolute ethanol was stirred and cooled to 0 °C with the addition of acid. The reaction solution was stirred for 2 h. Then rotary evaporation was applied to evaporate the solvent with a pressure of −0.1 MPa at 45 °C. The precipitate was washed three times with diethyl ether and dried under vacuum (60 °C, 5 h) for future use.

Fabrication of Hybrid $CH_3NH_3PbX_3$ QDs. Colloidal $CH_3NH_3PbX_3$ QDs were fabricated following the LARP technique, which is described in the following section. In a typical synthesis of $CH_3NH_3PbBr_3$ QDs, a mixture of 0.16 mmol CH_3NH_3Br and 0.2 mmol $PbBr_2$ was dissolved in 5 mL of DMF with 20 μL of *n*-octylamine and 0.5 mL of oleic acid to form a precursor solution. Two milliliters of precursor solution was dropped into 10 mL of toluene with vigorous stirring. Along with the mixing, strong green PL emission was observed. After centrifugation at 7000 rpm for 10 min to discard the precipitates, a bright yellow-green colloidal solution was obtained. $CH_3NH_3PbCl_3$ QDs and $CH_3NH_3PbI_3$ QDs were fabricated by varying the precursors and solvents following a similar LARP strategy. DMSO was used to dissolve $PbCl_2$ for the fabrication of $CH_3NH_3PbBr_{3-x}Cl_x$ QDs. Halide substitutions were performed by blending appropriate reagents ($PbCl_2$, $PbBr_2$, PbI_2, CH_3NH_3Br, CH_3NH_3Cl, and CH_3NH_3I) in the preparation of precursor solutions. To avoid fast degradation, the fabrication of iodide-substituted samples was accomplished in a glovebox. The solid powder of $CH_3NH_3PbBr_3$ QDs was obtained by fast evaporating the residual organic solvents on a hot plate at 100 °C. It is noted that the formation yield of $CH_3NH_3PbBr_3$ QDs is very limited due to the formation of large particles along with small-sized QDs.

Preparation of Micrometer-Sized $CH_3NH_3PbBr_3$ Particles. Micrometer-sized $CH_3NH_3PbBr_3$ particles were prepared following a reprecipitation method using a precursor solution made by dissolving 0.2 mmol CH_3NH_3Br and 0.2 mmol $PbBr_2$ into 5 mL of DMF solution. Then, the precursor solution was added dropwise into 10 mL of toluene, and the as-formed precipitates were collected and dried into powder for further characterizations.

Fabrication of LED Devices. The KSF powder was blended with silicone gel A and B followed by waiting for 30 min to let the silicone gel cure. The $CH_3NH_3PbBr_3$ QDs were dissolved into chloroform with PMMA. A layer of silicone gel with KSF was painted on the surface of the blue chip, followed by casting a layer of QDs in PMMA.

Characterizations. The XRD measurements were measured on a Bruker/D8 FOCUS X-ray diffractometer, using a Cu Kα radiation source (wavelength at 1.5405 Å). The samples were scanned from $3° < 2\theta < 60°$ at an increment of 2°/min. Liquid samples in toluene was deposited on amorphous carbon-coated copper grids, and the samples were analyzed using a JEOL-JEM 2100F TEM machine operating at an acceleration voltage of 200 kV. XPS determinations were carried out at a ULVAC-PHI machine (PHIQUANTERA-II SXM) with Al Kα as the X-ray source. EDS analyses were performed on a S-4800 microscope, working at 15 kV. UV−vis absorption spectra of QDs dissolved in toluene were measured on a UV-6100 UV−vis spectrophotometer (Shanghai Mapada Instruments Co., Ltd., China). PL spectra were taken using a F-380 fluorescence spectrometer (Tianjin Gangdong Sci. & Tech. Development Co., Ltd., China). Time-resolved PL measurement was collected using a fluorescence lifetime measurement system (C11367-11, Hamamatsu Photonics, Japan). Low-temperature-dependent PL spectra measurements were performed in the temperature range of 5−300 K using a liquid helium cooler. The high-temperature-dependent PL emissions were collected by the microscope system equipped with a GaN laser (405 nm) and an objective lens (LMU-20X-325, 50× magnification) on a T95-PE heating stage (Linkam Scientific Instruments Ltd.). The absolute PLQYs of diluted QD solutions were determined using a fluorescence spectrometer with an integrated sphere (C9920-02, Hamamatsu Photonics, Japan) excited at a wavelength of 450 nm using a blue LED light source.

Conflict of Interest: The authors declare no competing financial interest.

Acknowledgment. The authors would like to thank Dr. L. Lu and Mr. Q.C. Zhou for assistance with the LED device fabrication and characterization, Mr. N.B. Wang for the PL lifetime measurements and absolute PLQY determination, and Prof. J.B. Li for providing the facility for high-temperature-dependent spectroscopic measurements. This study was supported by The National Basic Research Program of China (Nos. 2013CB328804 and 2011CB933600), National Natural Science Foundation of China (Grant No. 21343005), Beijing Nova program (No. xx2014B040), and the Open Research Fund of State Key Laboratory of Bioelectronics Southeast University.

Supporting Information Available: XRD patterns, analyses of temperature-dependent PL spectra, description of halide-substituted QDs, and performance of as-fabricated pc-WLED devices. This material is available free of charge *via* the Internet at http://pubs.acs.org.

REFERENCES AND NOTES

1. Pust, P.; Weiler, V.; Hecht, C.; Tuecks, A.; Wochnik, A. S.; Henss, A. K.; Wiechert, D.; Scheu, C.; Schmidt, P. J.; Schnick, W. Narrow-Band Red-Emitting $Sr[LiAl_3N_4]:Eu^{2+}$ as a Next-Generation LED-Phosphor Material. *Nat. Mater.* **2014**, *13*, 891–896.
2. Li, G.; Fleetham, T.; Turner, E.; Hang, X. C.; Li, J. Highly Efficient and Stable Narrow-Band Phosphorescent Emitters for OLED Applications. *Adv. Opt. Mater.* **2015**, *3*, 390–397.
3. Sun, Q. J.; Wang, A.; Li, L. S.; Wang, D. Y.; Zhu, T.; Xu, J.; Yang, C. H.; Li, Y. F. Bright, Multicoloured Light-Emitting Diodes Based on Quantum Dots. *Nat. Photonics* **2007**, *1*, 717–722.
4. Shirasaki, Y.; Supran, G. J.; Bawendi, M. G.; Bulovic, V. Emergence of Colloidal Quantum-Dot Light-Emitting Technologies. *Nat. Photonics* **2013**, *7*, 13–23.
5. Kovalenko, M. V.; Manna, L.; Cabot, A.; Hens, Z.; Talapin, D. V.; Kagan, C. R.; Klimov, V. I.; Rogach, A. L.; Reiss, P.; Milliron, D. J.; et al. Prospects of Nanoscience with Nanocrystals. *ACS Nano* **2015**, *9*, 1012–1057.
6. Kojima, A.; Teshima, K.; Shirai, Y.; Miyasaka, T. Organometal Halide Perovskites as Visible-Light Sensitizers for Photovoltaic Cells. *J. Am. Chem. Soc.* **2009**, *131*, 6050–6051.
7. Lee, M. M.; Teuscher, J.; Miyasaka, T.; Murakami, T. N.; Snaith, H. J. Efficient Hybrid Solar Cells Based on

Meso-superstructured Organometal Halide Perovskites. *Science* **2012**, *338*, 643–647.
8. Cai, B.; Xing, Y. D.; Yang, Z.; Zhang, W. H.; Qiu, J. S. High Performance Hybrid Solar Cells Sensitized by Organolead Halide Perovskites. *Energy Environ. Sci.* **2013**, *6*, 1480–1485.
9. Luo, J.; Im, J. H.; Mayer, M. T.; Schreier, M.; Nazeeruddin, M. K.; Park, N. G.; Tilley, S. D.; Fan, H. J.; Graetzel, M. Water Photolysis at 12.3% Efficiency *via* Perovskite Photovoltaics and Earth-Abundant Catalysts. *Science* **2014**, *345*, 1593–1596.
10. Zhou, H. P.; Chen, Q.; Li, G.; Luo, S.; Song, T. B.; Duan, H. S.; Hong, Z. R.; You, J. B.; Liu, Y. S.; Yang, Y. Interface Engineering of Highly Efficient Perovskite Solar Cells. *Science* **2014**, *345*, 542–546.
11. Manser, J. S.; Kamat, P. V. Band Filling with Free Charge Carriers in Organometal Halide Perovskites. *Nat. Photonics* **2014**, *8*, 737–743.
12. D'Innocenzo, V.; Grancini, G.; Alcocer, M. J. P.; Kandada, A. R. S.; Stranks, S. D.; Lee, M. M.; Lanzani, G.; Snaith, H. J.; Petrozza, A. Excitons *versus* Free Charges in Organolead Trihalide Perovskites. *Nat. Commun.* **2014**, *5*, 3586.
13. Era, M.; Morimoto, S.; Tsutsui, T.; Saito, S. Organic–Inorganic Heterostructure Electroluminescent Device using a Layered Perovskite Semiconductor $(C_6H_5C_2H_4NH_3)_2PbI_4$. *Appl. Phys. Lett.* **1994**, *65*, 676–678.
14. Chondroudis, K.; Mitzi, D. B. Electroluminescence from an Organic–Inorganic Perovskite Incorporating a Quaterthiophene Dye within Lead Halide Perovskite Layers. *Chem. Mater.* **1999**, *11*, 3028–3030.
15. Dohner, E. R.; Jaffe, A.; Bradshaw, L. R.; Karunadasa, H. I. Intrinsic White-Light Emission from Layered Hybrid Perovskites. *J. Am. Chem. Soc.* **2014**, *136*, 13154–13156.
16. Xing, G. C.; Mathews, N.; Lim, S. S.; Yantara, N.; Liu, X.; Sabba, D.; Gratzel, M.; Mhaisalkar, S.; Sum, T. C. Low-Temperature Solution-Processed Wavelength-Tunable Perovskites for Lasing. *Nat. Mater.* **2014**, *13*, 476–480.
17. Tan, Z. K.; Moghaddam, R. S.; Lai, M. L.; Docampo, P.; Higler, R.; Deschler, F.; Price, M.; Sadhanala, A.; Pazos, L. M.; Credgington, D.; et al. Bright Light-Emitting Diodes Based on Organometal Halide Perovskite. *Nat. Nanotechnol.* **2014**, *9*, 687–692.
18. Deschler, F.; Price, M.; Pathak, S.; Klintberg, L. E.; Jarausch, D. D.; Higler, R.; Huettner, S.; Leijtens, T.; Stranks, S. D.; Snaith, H. J.; et al. High Photoluminescence Efficiency and Optically Pumped Lasing in Solution-Processed Mixed Halide Perovskite Semiconductors. *J. Phys. Chem. Lett.* **2014**, *5*, 1421–1426.
19. Stranks, S. D.; Burlakov, V. M.; Leijtens, T.; Ball, J. M.; Goriely, A.; Snaith, H. J. Recombination Kinetics in Organic–Inorganic Perovskites: Excitons, Free Charge, and Subgap States. *Phys. Rev. Appl.* **2014**, *2*, 034007.
20. Kojima, A.; Ikegami, M.; Teshima, K.; Miyasaka, T. Highly Luminescent Lead Bromide Perovskite Nanoparticles Synthesized with Porous Alumina Media. *Chem. Lett.* **2012**, *41*, 397–399.
21. D'Innocenzo, V.; Srimath Kandada, A. R.; De Bastiani, M.; Gandini, M.; Petrozza, Y. Tuning the Light Emission Properties by Band Gap Engineering in Hybrid Lead Halide Perovskite. *J. Am. Chem. Soc.* **2014**, *136*, 17730–17733.
22. Noel, N. K.; Abate, A.; Stranks, S. D.; Parrott, E. S.; Burlakov, V. M.; Goriely, A.; Snaith, H. J. Enhanced Photoluminescence and Solar Cell Performance *via* Lewis Base Passivation of Organic–Inorganic Lead Halide Perovskites. *ACS Nano* **2014**, *8*, 9815–9821.
23. Queisser, H. J.; Haller, E. E. Defects in Semiconductors: Some Fatal, Some Vital. *Science* **1998**, *281*, 945–950.
24. Yin, W. J.; Shi, T.; Yan, Y. Unusual Defect Physics in $CH_3NH_3PbI_3$ Perovskite Solar Cell Absorber. *Appl. Phys. Lett.* **2014**, *104*, 063903.
25. Agiorgousis, M. L.; Sun, Y. Y.; Zeng, H.; Zhang, S. Strong Covalency-Induced Recombination Centers in Perovskite Solar Cell Material $CH_3NH_3PbI_3$. *J. Am. Chem. Soc.* **2014**, *136*, 14570–14575.
26. Cassette, E.; Mirkovic, T.; Scholes, G. D. Toward the Control of Nonradiative Processes in Semiconductor Nanocrystals. *J. Phys. Chem. Lett.* **2013**, *4*, 2091–2093.
27. Nirmal, M.; Brus, L. Luminescence Photophysics in Semiconductor Nanocrystals. *Acc. Chem. Res.* **1999**, *32*, 407–414.
28. Schmidt, L. C.; Pertegas, A.; Gonzalez-Carrero, S.; Malinkiewicz, O.; Agouram, S.; Minguez Espallargas, G.; Bolink, H. J.; Galian, R. E.; Perez-Prieto, J. Nontemplate Synthesis of $CH_3NH_3PbBr_3$ Perovskite Nanoparticles. *J. Am. Chem. Soc.* **2014**, *136*, 850–852.
29. Protesescu, L.; Yakumin, S.; Bodnarchuk, M. I.; Krieg, F.; Caputo, R.; Hendon, C. H.; Yang, R. X.; Walsh, A.; Kovalenko, M. C. Nanocrystals of Cesium Lead Halide Perovskites ($CsPbX_3$, X = Cl, Br, and I): Novel Optoelectronic Materials Showing Bright Emission with Wide Color Gamut. *Nano Lett.* **2015**, 10.1021/nl5048779.
30. Tanaka, K.; Takahashi, T.; Ban, T.; Kondo, T.; Uchida, K.; Miura, N. Comparative Study on the Excitons in Lead-Halide-Based Perovskite-Type Crystals $CH_3NH_3PbBr_3$ and $CH_3NH_3PbI_3$. *Solid State Commun.* **2003**, *127*, 619–623.
31. Zhao, Y. S.; Fu, H. B.; Peng, A. D.; Ma, Y.; Xiao, D. B.; Yao, J. N. Low-Dimensional Nanomaterials Based on Small Organic Molecules: Preparation and Optoelectronic Properties. *Adv. Mater.* **2008**, *20*, 2859–2876.
32. Kasai, H.; Nalwa, H. S.; Oikawa, H.; Okada, S.; Matsuda, H.; Minami, N.; Kakuta, A.; Ono, K.; Mukoh, A.; Nakanishi, H. A Novel Preparation Method of Organic Microcrystals. *Jpn. J. Appl. Phys.* **1992**, *31*, L1132.
33. Niu, Y. W.; Zhang, F.; Bai, Z. L.; Dong, Y. P.; Yang, J.; Liu, R. B.; Zou, B. S.; Li, J. B.; Zhong, H. Z. Aggregation-Induced Emission Features of Organometal Halide Perovskites and Their Fluorescence Probe Applications. *Adv. Opt. Mater.* **2014**, *3*, 112–119.
34. Pradhan, N.; Reifsnyder, D.; Xie, R. G.; Aldana, J.; Peng, X. G. Surface Ligand Dynamics in Growth of Nanocrystals. *J. Am. Chem. Soc.* **2007**, *129*, 9500–9509.
35. Yin, Y. D.; Alivisatos, A. P. Colloidal Nanocrystal Synthesis and the Organic–Inorganic Interface. *Nature* **2005**, *437*, 664–670.
36. Jeon, N. J.; Noh, J. H.; Kim, Y. C.; Yang, W. S.; Ryu, S.; Il Seol, S. Solvent Engineering for High-Performance Inorganic–Organic Hybrid Perovskite Solar Cells. *Nat. Mater.* **2014**, *13*, 897–903.
37. Jasieniak, J.; Mulvaney, P. From Cd-Rich to Se-Rich: The Manipulation of CdSe Nanocrystal Surface Stoichiometry. *J. Am. Chem. Soc.* **2007**, *129*, 2841–2848.
38. Sykora, M.; Koposov, A. Y.; McGuire, J. A.; Schulze, R. K.; Tretiak, O.; Pietryga, J. M.; Klimov, V. I. Effect of Air Exposure on Surface Properties, Electronic Structure, and Carrier Relaxation in PbSe Nanocrystals. *ACS Nano* **2010**, *4*, 2021–2034.
39. Hines, D. A.; Kamat, P. V. Recent Advances in Quantum Dot Surface Chemistry. *ACS Appl. Mater. Interfaces* **2014**, *6*, 3041–3057.
40. Zhang, M.; Yu, H.; Lyu, M.; Wang, Q.; Yun, J. H.; Wang, L. Z. Composition-Dependent Photoluminescence Intensity and Prolonged Recombination Lifetime of Perovskite $CH_3NH_3PbBr_{3-x}Cl_x$ Films. *Chem. Commun.* **2014**, *50*, 11727–11730.
41. Wang, X. Y.; Qu, L. H.; Zhang, J. Y.; Peng, X. G.; Xiao, M. Surface-Related Emission in Highly Luminescent CdSe Quantum Dots. *Nano Lett.* **2003**, *3*, 1103–1106.
42. Zhao, Y.; Riemersma, C.; Pietra, F.; Koole, R.; Donegá, C. d. M.; Meijerink, A. High-Temperature Luminescence Quenching of Colloidal Quantum Dots. *ACS Nano* **2012**, *6*, 9068–9067.
43. Wu, K.; Bera, A.; Ma, C.; Du, Y. M.; Yang, Y.; Li, L.; Wu, T. Temperature-Dependent Excitonic Photoluminescence of Hybrid Organometal Halide Perovskite Films. *Phys. Chem. Chem. Phys.* **2014**, *16*, 22476–22481.
44. Dey, P.; Paul, J.; Bylsma, J.; Karaiskaj, D.; Luther, J.; Beard, M.; Romero, A. Origin of the Temperature Dependence of the Bandgap of PbS and PbSe Quantum Dots. *Solid State Commun.* **2013**, *165*, 49–54.

45. Quarti, C.; Grancini, G.; Mosconi, E.; Bruno, P.; Ball, J. M.; Lee, M. M.; Snaith, H. J.; Petrozza, A.; Angelis, F. D. The Raman Spectrum of the $CH_3NH_3PbI_3$ Hybrid Perovskite: Interplay of Theory and Experiment. *J. Phys. Chem. Lett.* **2014**, *5*, 279–284.
46. Diroll, T. B.; Murray, C. B. High-Temperature Photoluminescence of CdSe/CdS Core/Shell Nanoheterostructures. *ACS Nano* **2014**, *8*, 6466–6474.
47. Kim, Y. H.; Cho, H.; Heo, J. H.; Kim, T. S.; Myoung, N.; Lee, C. L.; Im, S. H.; Lee, T. W.; Kim, Y. H.; Cho, H.; et al. Multicolored Organic/Inorganic Hybrid Perovskite Light-Emitting Diodes. *Adv. Mater.* **2015**, *27*, 1248–1254.
48. Jang, E.; Jun, S.; Jang, H.; Llim, J.; Kim, B.; Kim, Y. White-Light-Emitting Diodes with Quantum Dot Color Converters for Display Backlights. *Adv. Mater.* **2010**, *22*, 3076–3080.
49. Scholes, G. D.; Rumbles, G. Excitons in Nanoscale Systems. *Nat. Mater.* **2006**, *5*, 683–696.